

Parallel Quantum Simulation of Large Systems on Small NISQ Computers

F. Barratt,¹ James Dborin,² Matthias Bal,³ Vid Stojevic,³ Frank Pollmann,⁴ and A. G. Green²

¹*Department of Mathematics, King's College London, Strand, London WC2R 2LS, United Kingdom*

²*London Centre for Nanotechnology, University College London,
Gordon St., London, WC1H 0AH, United Kingdom*

³*GTN Limited, Clifton House, 46 Clifton Terrace,
Finsbury Park, London N4 3JP, United Kingdom*

⁴*Department of Physics, T42, Technische Universität München,
James-Frank-Straße 1, D-85748 Garching, Germany*

(Dated: June 10, 2022)

Tensor networks permit computational and entanglement resources to be concentrated in interesting regions of Hilbert space. Implemented on NISQ machines they allow simulation of quantum systems that are much larger than the computational machine itself. This is achieved by parallelising the quantum simulation. Here, we demonstrate this in the simplest case; an infinite, translationally invariant quantum spin chain. We provide Cirq and Qiskit code that translate infinite, translationally invariant matrix product state (iMPS) algorithms to finite-depth quantum circuit machines, allowing the representation, optimisation and evolution arbitrary one-dimensional systems. Illustrative simulated output of these codes for achievable circuit sizes is given.

I. INTRODUCTION

The insight underpinning Steve White's formulation of the density matrix renormalisation group (DMRG) is that entanglement is the correct resource to focus upon to formulate accurate, approximate descriptions of large quantum systems[1]. Later understood as an algorithm to optimise a matrix product state (MPS)[2], this notion underpins the use of tensor networks as a variational parametrisation of wavefunctions with quantified entanglement resource. Such approaches allow one to concentrate computational resources in the appropriate region of Hilbert space and provide an effective and universal way to simulate quantum systems [3, 4]. They also provide an effective framework to distribute entanglement resources in simulation on noisy intermediate scale quantum (NISQ) computers.

Quantum computers such as those of Google, Rigetti, IBM and others implement finite-depth quantum circuits with controllable local two-qubit unitary gates. Innovations for quantum simulation include using these circuits as variational wavefunctions[5], optimising them stochastically or by phase estimation[6], and evolving them either by accurate Trotterisation of the evolution operator[7–9] or variationally[10]. Currently available NISQ devices are limited by gate fidelity and the resultant restriction of available entanglement resources. Since the finite-depth quantum circuit may be equivalently described as a tensor network[11], tensor networks provide a convenient framework with which to distribute entanglement to the useful regions of Hilbert space and to make efficient use of this relatively scarce resource.

We dub the implementation of a tensor network on such a NISQ device a *Quantum tensor network*. There are several advantages to this framework. It fits directly into a broader ecosystem of classical simulation of quantum systems. Indeed, because it is based upon the manipulation of explicitly unitary elements, the quantum circuit provides perhaps the most natural realisation of tensor networks. Canonicalisation at each step in a classical tensor network calculation amounts to reducing the tensors to isometries — a step that is not required in an explicitly unitary realisation. Moreover, the remaining elements of unitaries parametrise the tangent space of the variational manifold[12, 13].

Here we demonstrate that quantum tensor networks can be used to parallelise quantum simulation of systems that are much larger than available NISQ machines[14]. Central to this is dividing the quantum system into a number of sub-elements that are weakly-entangled and can be simulated in parallel on different circuits. The influence of the different regions of the system upon one another can be summarised by an effective state on a much smaller number of quantum bits. We provide Cirq and Qiskit code for the simplest class of examples — infi-

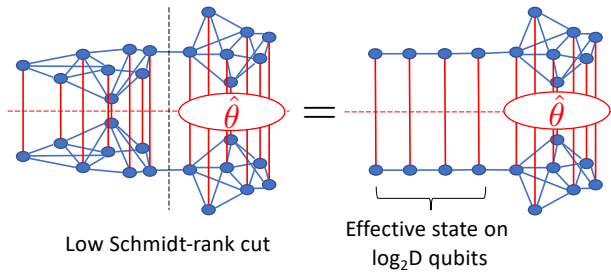


FIG. 1. **Tensor network for a quantum state that is weakly entangled across a certain partition.** This weak entanglement allows parallel simulation of the two partitions of the system. The expectation of an operator located to the right of the partition can be carried out by replacing the state on the left by a state over much fewer spins (the number determined by the entanglement across the cut). The numerical values of correlations in this smaller representation of the left are determined by quantum effects in the full left hand system, and can be computed in parallel and iterated to consistency.

nite, translationally invariant quantum spin chains. This is a direct translation (*mutatis mutandis*) of iMPS algorithms to quantum circuit machines. The remarkably simple circuits revealed below allow the representation of an infinite quantum state, and its optimisation and real-time evolution for a given Hamiltonian.

II. PARALLEL QUANTUM SIMULATION ACROSS WEAKLY-ENTANGLED CUTS

To parallelise our simulation on a small NISQ machine, we first identify partitions of the system where the effect of one partition upon the other can be summarised by a small amount of information. This is achieved by making Schmidt decompositions across the cut: $|\psi\rangle = \sum_{\alpha=1}^D \lambda^\alpha |\phi_L^\alpha\rangle |\phi_R^\alpha\rangle$, where $|\phi_L^\alpha\rangle$ are an orthonormal set of states to the left of the cut and $|\phi_R^\alpha\rangle$ the same on the right. The λ^α are known as the Schmidt coefficients and D the Schmidt rank or bond order. Retaining λ^α only above some threshold value provides a way to compress representations of a quantum state; the MPS construction can be obtained by applying this procedure sequentially along a spin chain[4].

If an observation is made on the right-hand-side of such a cut, the effect of the quantum state on the left upon the observation can be summarised by just D^2 variables. This same effect can be achieved by an effective state on a spin chain of length $\log_2 D$ — see Fig. 1 — which can be parametrised on the quantum circuit by an $SU(D^2)$ unitary V_L . The precise numerical values must be determined by solving a quantum mechanical problem on the left of the system. Similarly for observations made to the left of the cut, the effect of the right-hand side can be summarised by a unitary V_R .

This gives a prescription for parallel quantum simulation. Calculations of the quantum wavefunction to the left and right of the cut can be carried out on different quantum circuits or sequentially on the same circuit. The effects of the left partition upon the right partition and *vice versa* — through the environment unitaries V_L and V_R — are iterated to consistency. At each stage of this iteration, measurements must be performed in order to determine $V_{L/R}$. The small Schmidt rank of the cut reduces the computational complexity of this process - if we were to do full state tomography, to $\mathcal{O}(\text{poly}(D))$, but with more sophisticated methods even to $\mathcal{O}(\log(D))$, as in the example in the following section.

There are many physical situations in which this parallelisation might be useful. For example, large organic molecules that have localised chemical activity — this activity may be modulated or tuned by the surrounding parts of the molecule and the interplay of these effects could be calculated in parallel. In the following, inspired by iMPS tensor networks, we give quantum circuits that embody these ideas.

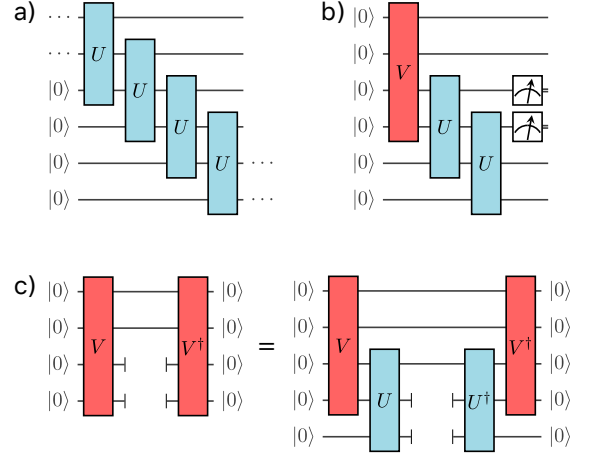


FIG. 2. **Quantum circuits for translationally invariant states and their local measurement.** a) An infinite depth and width quantum circuit representing a translationally invariant state. $U \in SU(dD)$ with d the local Hilbert space dimension and $D = 2^N$ the bond order. $d = 2$ for spin 1/2 and is used exclusively throughout this paper. In these illustrations $D = 4$. The circuit acts upon a reference state $|000\dots\rangle$ at the left of the figure with unitary operators applied sequentially reading left to right. b) Local measurements on this translationally invariant state can be reproduced exactly by the finite circuit shown. The reduced form takes advantage of the unitarity of U , due to which sites to the left of the observable do not contribute. The environment unitary $V \equiv V(U) \in SU(D^2)$ summarises the effect of sites to the right of the observable and describes an effective state over $N = \log_2 D$ spins. c) The environment unitary $V(U)$ is the solution of the fixed point equation shown. This equation is to be interpreted as an equality of the reduced density matrices implied by the free qubit lines. We show in the Methods how to implement this using swap gates.

III. PARALLEL SIMULATION WITH QUANTUM TENSOR NETWORKS

Representing the state: A translationally invariant, spin 1/2 MPS state of bond order $D = 2^N$ can be represented by the infinite circuit shown in Fig.2 a). Expectations of local operators in this state can be evaluated by the finite circuit shown in Fig.2 b). The effect of contracting the infinite circuit to the left of the operator is trivial due to the unitarity of $U \in SU(2D)$ (which automatically encodes the left canonical form of the related MPS tensor). The contraction to the right is described by the tensor $V \in SU(D^2)$, which encodes an effective state over $N = \log_2 D$ spins and their entanglement with the remaining system to the left-hand side. This unitary is determined self-consistently from U by the circuit shown in Fig.2 c). The operation of such a circuit at $D = 2$ was demonstrated in Ref.[15] on an IBM quantum circuit, where analytic forms were known for both U and V along a line through the phase diagram of a model with topological phase transition. In general, $V \equiv V(U)$ is not known and must be solved following Fig. 2 c).

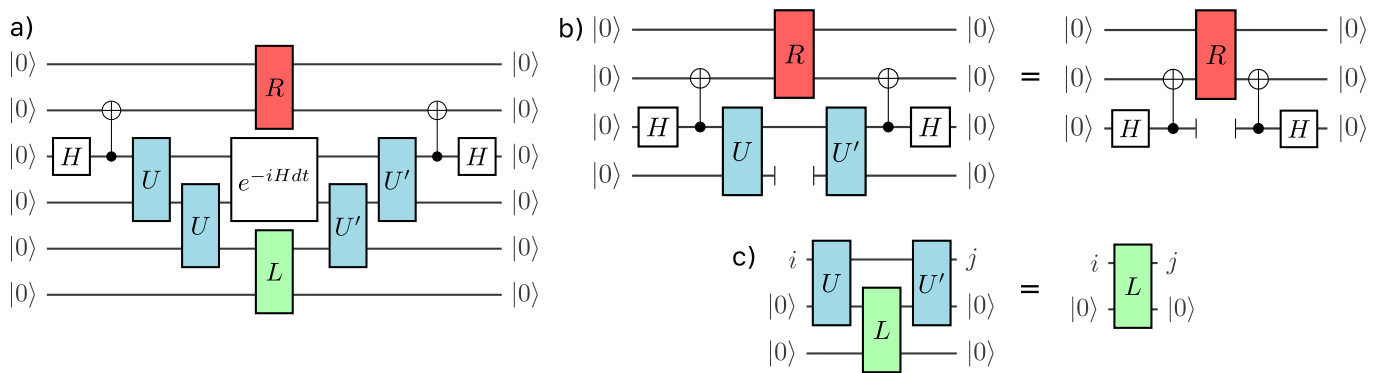


FIG. 3. **Quantum Implementation of the Time-dependent variational principle.** For simplicity, we depict the above circuits for $D = 2$. Higher bond order cases are given in the supplementary materials. a) The unitary U' that optimises the overlap of this circuit with $|000\dots\rangle$ describes the time evolution of the state described by $U(t)$ by a time interval dt under the Hamiltonian \mathcal{H} , i.e. $U' = U(t + dt)$. b) and c) The mixed environment unitaries R and L are given by the fixed point solutions of these circuit equations. As in Fig.2, these are to be interpreted as an equality of the density matrices implied by free qubit lines.

Optimising the state: We can find the ground state and the corresponding energy density of translationally invariant Hamiltonians by minimizing the expectation value of the energy. The algorithm mirrors the variational quantum eigensolver. The expectation of the local Hamiltonian is found by measuring the corresponding Pauli strings on the physical qubits (see Fig. 2b)). The result can then be minimised as a function of the ansatz parameters. Updates must be interleaved with updates to the environment, V , such that we optimize over valid translationally invariant states.

Evolving the state: Perhaps the most compelling feature of this implementation is the ease with which time-evolution can be achieved. The simple circuit shown in Fig. 3 a) returns the unitary $U' \equiv U(t + dt)$ that updates the state encoded by $U(t)$ to a time $t + dt$ under evolution with the Hamiltonian \mathcal{H} . The first variation of this circuit with respect to U' returns the time-dependent variational principle for iMPS in the form first presented by Haegeman *et al.* in Ref. [12]. The equivalence uses the automatic encoding of the gauge-fixing of the state to canonical form as well as encoding of the tangent space and its gauge fixing (see Methods section and additional notes in Supplementary Materials). As in the determination of the best groundstate approximation above, the update involves two nested loops; one to find the update U' and one to find the environment tensors $L \equiv L(U, U')$ and $R \equiv R(U, U')$ — both of which are required in this case as the circuit corresponds to the overlap of two different states rather than expectations taken in a given state. We have used a slightly different way of representing these environments in Fig. 3 compared to that employed in Fig. 2.

Quantum Advantage: It is natural to ask whether there is any quantum advantage from using a quantum circuit in this way. Algorithms for manipulating iMPS (iDMRG,

TDVP, etc.) [3, 16, 17] are classically efficient - they have complexity of $\mathcal{O}(D^3)$. Where then is the room for improvement by implementation on a quantum circuit? The quantum advantage comes from the potentially exponential reduction in the dependence upon the bond dimension, D .

In a quantum circuit, the multi-qubit unitaries must be compiled to the available gate set. An arbitrary element of $SU(D)$, required to implement an iMPS of bond dimension D , requires $\mathcal{O}(D)$ gates [18] and so there is no (exponential) quantum advantage. However, a subset of non-trivial elements with entanglement S that would require a bond dimension $D \exp(S)$ can be achieved with circuits whose depth is $S \log D$ giving an exponential speedup over the classical implementation[19]. This reduces the contraction time from $\mathcal{O}(D^3)$ for a typical classical implementation to $\mathcal{O}(\log D)$ in the quantum case.

IV. RESULTS

We have written Cirq and Qiskit code to implement the quantum circuits shown in Figs. 2 and 3. The results of running this code in simulation on Google's Cirq simulator are shown in Fig. 4. We have chosen optimisation and time evolution of the transverse field Ising model[21], and Poincare sections of the dynamics of the PXP Hamiltonian[22] as illustrative examples. The properties of the transverse field Ising model are well understood. The Loschmidt echo (fidelity of the time-evolved wavefunction with the initial wavefunction) reveals a dynamical phase transition[21] which provides a non-trivial test for our simulation. Our main findings are as follows: i. When run without gate errors and complete representation of the unitaries U, V, L , and R , our code precisely reproduces the optimum iMPS and its time evolution using the time-dependent variational principle.

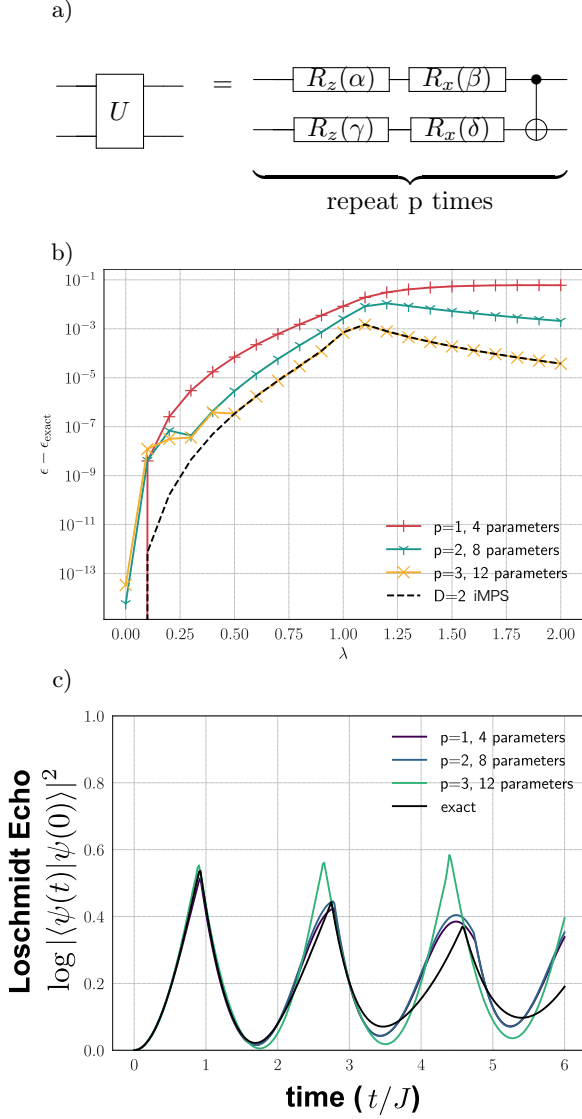


FIG. 4. Results of simulating the transverse field Ising model: The Hamiltonian $\mathcal{H} = \sum_n [\hat{\sigma}_n^z \hat{\sigma}_{n+1}^z + \lambda \hat{\sigma}_n^x]$ is studied with a bond order $D = 2$ quantum matrix product state. a) The $SU(4)$ unitaries U and V are compiled to the circuit as shown. The parameter p is varied to increase the accuracy. Although more efficient parametrizations exist for 2 qubit unitaries[20], as well as circuits more specifically tuned to this problem, we choose a generic circuit. It is readily extendible to higher bond orders [see Supplementary Materials]. b) The optimum state is found using the circuits depicted in Fig. 2. The energy of this state is a better approximation to the true groundstate energy as the depth of parametrization increases and converges to that obtained in a conventional MPS algorithm. In particular, we have checked that the parametrization of Ref.[20] perfectly reproduces the MPS results. Note that at $\lambda = 0$ the Hamiltonian is optimised by a product state, which is captured perfectly with $p = 1$. c) Transverse field Ising model displays dynamical phase transitions in the Loschmidt echo[21]. These are revealed in the simulated runs of the quantum time-dependent variational principle embodied by the circuits in Fig.3. More accurate circuits are required to obtain good agreement. The results indicated as exact in the above are exact analytical results.

ii. Factorisations of the unitaries reduce the fidelity of our results. These are systematically improved as the depth or expressibility of the ansatz is increased. Full parametrisations of the unitaries reproduce classical MPS results exactly.

iii. Going from representing, to optimising, to time-evolving states places increasing demands upon circuit-depth and width. Accurate results require increasingly deep factorisation of the unitaries, and suffer increasingly adverse effects of gate errors.

Fig. 5 demonstrates the results of running our quantum time-dependent variational principle code on the PXP model[23]. It reproduces the Poincare maps similar to those of Ref.[22]. Such plots have advantages for NISQ machines as they permit the use of error mitigation schemes. To produce Fig. 5 we have used post-selection over energy to discard erroneous points in the Poincare map. This mitigates both integration errors due to the finite time-step, stochastic optimisation, and potentially errors due to finite gate fidelity. Structures within the Poincare map, while distorted by errors, are nevertheless robust to them.

V. DISCUSSION

We have presented a new way to perform quantum simulations by translating tensor network algorithms to quantum circuits. Our approach allows parallel quantum simulations of large systems on small NISQ computers. We have demonstrated this for one-dimensional translationally invariant spin chains. The translation of MPS algorithms naturally encodes fundamental features of matrix product states and the tangent space to the variational manifold that they form. In demonstrating the operation of such circuits, we have touched upon some immediate questions including the expressiveness of shallow circuit restrictions of tensor network states, their effect upon simulation alongside that of finite gate fidelity. These warrant further systematic study.

Our algorithms are readily extensible to inhomogeneous one-dimensional systems and to higher dimensions following existing methods that wrap one-dimensional states to higher dimensional systems[16, 17]. It would be interesting to study other gauge restrictions of MPS — such as the mixed gauge of modern classical time-dependent variational principle codes — which can also be implemented in quantum circuits. Generalisations of MPS that more directly describe higher dimensional systems are also available. For example, the projected entangled pair states (PEPS) give a two-dimensional generalisation. In realising these states on a quantum circuit, they must be formed from isometric tensors. Until recently, a suitable canonical form for PEPS was not available. The isometric version of PEPS presented in Ref.[25] shows great promise and ought to be possible to implement on a suitably connected quantum circuit. Other tensor networks such as the multi-scale entangle-

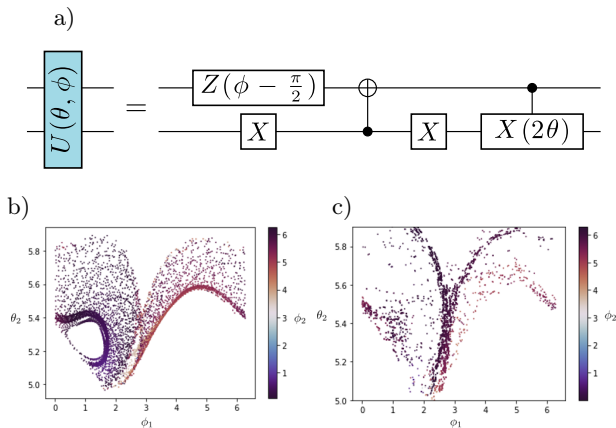


FIG. 5. **Many Body Scars in the PXP model:** The Hamiltonian $\mathcal{H} = \sum_n (1 - \hat{\sigma}_{n-1}^z) \hat{\sigma}_n^x (1 - \hat{\sigma}_{n+1}^z)$, first posited to describe the results of quantum simulations using Rydberg atoms[23], displays a curious property known as many-body scarring[24], whereby from certain starting states, persistent oscillations that can be described with a low bond-order MPS are found. These are amenable to study on a NISQ machine using the quantum time-dependent variational principle of Fig 3. a) A simple set of 2-site periodic states at bond order $D = 2$ are parametrized by circuits with just 2 parameters per site, so 4 in total. b) A partial Poincaré section through the plane $\theta_1 = 0.9$ produced from a classical simulation using the matrix product state equations of motion presented in Ref.[22]. Initial conditions are chosen on a constant energy surface $\langle \mathcal{H} \rangle = 0$. The partial plot was produced with initial conditions along a line with spacing $\delta\phi_1 = 3 \times 10^{-2}$, with $\theta_1 = 0.9$ and $\theta_2 = 5.41$. The final parameter, ϕ_3 , chosen to fix the energy. c) The same Poincaré map produced simulating the quantum time-dependent variational principle in Cirq. We employ a simple error mitigation scheme dividing the Poincaré map into four regimes and post-selecting the 10% of trajectories with the lowest error in energy in each [see Supplementary Materials for further details]. While the figure is blurred somewhat by integration, the main features are still apparent

ment renormalisation ansatz [26] (MERA) are naturally based upon unitary operators and can be realised on a quantum circuit[27]. Indeed, MERA has been deployed for image classification on a small quantum circuit[28] and as a quantum convolutional neural network[29].

The tensor network framework also provides a convenient route to harness potential quantum advantage in simulation. The one-dimensional matrix product state ansatz is efficiently contractible. The time taken to calculate the expectation of a local operator scales proportional to the length of the system. A quantum imple-

mentation has the advantage of a potentially exponential decrease in the prefactor to this scaling. While a classical tensor network may efficiently represent the important correlations of quantum state in higher dimensions, its properties may not be efficiently contractible. Contraction of a PEPS state is provably NP hard[30]. In these circumstances circuit representations may give an exponential enhancement to the scaling of contraction not just to its pre-factor. However, the balance of advantage and cost can be delicate; extracting the elements of the tensors is easy classically, but quantum mechanically requires tomography of the circuit state, which is exponentially slow in the number of spins measured. This may be the bottleneck in hybrid algorithms[31]. Using the tensor network framework to distribute entanglement resources over the Hilbert space appropriately can mitigate some of these costs.

This work demonstrates the utility of translating tensor network algorithms to quantum circuits and opens a new and unexplored direction of quantum simulation. Potentially all of the advances of classical simulation of quantum systems using tensor networks can be translated in this way. Moreover, it provides a new perspective on classical algorithms suggesting related benefit in purely unitary implementations[32].

VI. ACKNOWLEDGEMENTS AND CONTRIBUTIONS

JD, FB and AGG were supported by the EPSRC through grants EP/L015242/1, EP/L015854/1 and EP/S005021/1. FP is funded by the European Research Council (ERC) under the European Unions Horizon 2020 research and innovation program (grant agreement No. 771537). FP acknowledges the support of the DFG Research Unit FOR 1807 through grants no.PO 1370/2-1, TRR80, and the Deutsche Forschungsgemeinschaft (DFG, German Research Foundation) under Germany's Excellence Strategy EXC-2111-390814868. We would like to acknowledge discussions with Adam Smith and Bernard Jobst, and GoogleAI for supporting attendance of FB at a Cirq coding workshop. AGG conceived the project and developed it initially with VS and MB. FB, JD and AGG worked out the detailed mapping of these ideas to a quantum circuit, wrote the Cirq and Qiskit code and ran the simulations. FP made key contributions at various points in the code development. The manuscript was written by FB, JD and AGG.

[1] S. R. White, Physical Review Letters **69**, 2863 (1992).
[2] S. Östlund and S. Rommer, Physical Review Letters **75**, 3537 (1995).

[3] D. Perez-Garcia, F. Verstraete, M. M. Wolf, and J. I. Cirac, Quantum Info. Comput. **7**, 401 (2007).
[4] G. Vidal, Phys. Rev. Lett. **91**, 147902 (2003).

- [5] A. Peruzzo, J. McClean, P. Shadbolt, M.-H. Yung, X.-Q. Zhou, P. J. Love, A. Aspuru-Guzik, and J. L. O’Brien, *Nature Communications* **5**, 4213 (2014).
- [6] A. Y. Kitaev, (1995), arXiv:quant-ph/9511026.
- [7] H. F. Trotter, *Proceedings of the American Mathematical Society* **10**, 545 (1959).
- [8] M. Suzuki, *Physics Letters A* **180**, 232 (1993).
- [9] M. B. Hastings, D. Wecker, B. Bauer, and M. Troyer, arXiv preprint arXiv:1403.1539 (2014).
- [10] Y. Li and S. C. Benjamin, *Physical Review X* **7**, 021050 (2017).
- [11] C. Schön, K. Hammerer, M. M. Wolf, J. I. Cirac, and E. Solano, *Phys. Rev. A* **75**, 032311 (2007).
- [12] J. Haegeman, J. I. Cirac, T. J. Osborne, I. Pižorn, H. Verschelde, and F. Verstraete, *Phys. Rev. Lett.* **107**, 070601 (2011).
- [13] A. G. Green, C. A. Hooley, J. Keeling, and S. H. Simon, (2016), arXiv:1607.01778.
- [14] T. Peng, A. Harrow, M. Ozols, and X. Wu, arXiv preprint arXiv:1904.00102 (2019).
- [15] A. Smith, B. Jobst, A. G. Green, and F. Pollmann, <http://arxiv.org/abs/1910.05351v2>.
- [16] R. Orús, *Annals of Physics* **349**, 117 (2014).
- [17] U. Schollwöck, *Annals of Physics* **326**, 96 (2011), january 2011 Special Issue.
- [18] M. A. Nielsen and I. L. Chuang, *Quantum Computation and Quantum Information: 10th Anniversary Edition*, 10th ed. (Cambridge University Press, USA, 2011).
- [19] M. Cerezo, A. Sone, T. Volkoff, L. Cincio, and P. J. Coles, arXiv preprint arXiv:2001.00550 (2020).
- [20] F. Vatan and C. Williams, *Physical Review A* **69**, 032315 (2004).
- [21] M. Heyl, A. Polkovnikov, and S. Kehrein, *Phys. Rev. Lett.* **110**, 135704 (2013).
- [22] A. Michailidis, C. Turner, Z. Papić, D. Abanin, and M. Serbyn, arXiv preprint arXiv:1905.08564 (2019).
- [23] C. J. Turner, A. A. Michailidis, D. A. Abanin, M. Serbyn, and Z. Papić, *Nature Physics* **14**, 745 (2018).
- [24] C. J. Turner, A. A. Michailidis, D. A. Abanin, M. Serbyn, and Z. Papić, *Nature Physics* **14**, 745 (2018).
- [25] M. P. Zaletel and F. Pollmann, (2019), arXiv:1902.05100.
- [26] G. Vidal, *Phys. Rev. Lett.* **101**, 110501 (2008).
- [27] I. H. Kim and B. Swingle, arXiv preprint arXiv:1711.07500 (2017).
- [28] E. Grant, M. Benedetti, S. Cao, A. Hallam, J. Lockhart, V. Stojevic, A. G. Green, and S. Severini, *npj Quantum Information* **4**, 65 (2018).
- [29] I. Cong, S. Choi, and M. D. Lukin, *Nature Physics* **15**, 1273 (2019).
- [30] N. Schuch, M. M. Wolf, F. Verstraete, and J. I. Cirac, *Physical review letters* **98**, 140506 (2007).
- [31] D. Wecker, M. B. Hastings, and M. Troyer, *Physical Review A* **92**, 042303 (2015).
- [32] A. G. Green and F. Pollmann, (2020).
- [33] C. Schön, E. Solano, F. Verstraete, J. I. Cirac, and M. M. Wolf, *Physical review letters* **95**, 110503 (2005).
- [34] W. Huggins, P. Patil, B. Mitchell, K. B. Whaley, and E. M. Stoudenmire, *Quantum Science and Technology* **4**, 024001 (2019).
- [35] S. Gopalakrishnan and A. Lamacraft, *Phys. Rev. B* **100**, 064309 (2019).
- [36] S.-J. Ran, arXiv preprint arXiv:1908.07958 (2019).
- [37] M. Ostaszewski, E. Grant, and M. Benedetti, (2019), arXiv:1905.09692.
- [38] J. C. Garcia-Escartin and P. Chamorro-Posada, *Phys. Rev. A* **87**, 052330 (2013).
- [39] F. Pollmann and A. M. Turner, *Phys. Rev. B* **86**, 125441 (2012).
- [40] A. A. Michailidis, C. J. Turner, Z. Papić, D. A. Abanin, and M. Serbyn, (2019), arXiv:1905.08564.

Appendix A: Methods

1. Quantum Matrix Product States

The mapping from MPS to quantum circuits that we use automatically embodies much of the variational manifold and its tangent space. The parsimony of this mapping to the quantum circuit suggests that it is the natural home for MPS. The fundamental building block of the circuits depicted in Figs. 2, 3 is the MPS tensor. A tensor of bond order D and local Hilbert space dimension d is represented by an $SU(dD)$ matrix following [13, 33–36] $A_{ij}^\sigma = U_{(1\otimes j),(\sigma\otimes i)}$ as shown in Fig.6. This translation automatically encodes the left canonical form of the MPS tensor; $\sum_\sigma (A^\sigma)_{ij}^\dagger A_{jk}^\sigma = \delta_{ik}$. This follows directly from the unitary property of U . A classical implementation of an MPS algorithm involves returning the tensors to this form after each step in an algorithm using singular value decompositions — in a quantum algorithm, such a manipulation is not required.

Moreover, the remaining elements of the unitary encode the tangent space structure to the sub-manifold of states spanned by MPS. These are important in constructing the projected Hamiltonian dynamics. Adopting the notation of Ref.[12], $V_{(\sigma\otimes\delta\neq 1),(i\otimes j)} = U_{(\delta\neq 1\otimes j),(\sigma\otimes i)}$ and automatically satisfies the null or tangent gauge-fixing condition $\sum_\sigma (A^\sigma)_{ij}^\dagger V_{jk}^{\sigma,\delta\neq 1} = 0$. This structure is responsible for the very compact quantum implementation of the time-dependent variational principle shown in Fig. 3. It obviates the need to calculate the tangent space structure at each step[12].

2. The Quantum Time-dependent Variational Principle

The equivalence with the classical implementation of the time-dependent variational principle for matrix product states and its quantum version can be seen by adopting the following parametrization of the updated unitary in the form

$$U' = U \exp \begin{pmatrix} 0 & X^\dagger \\ X & 0 \end{pmatrix}.$$

Taking the explicit overlap of the circuit in Fig. 3 a) with the state $|000\dots\rangle$ and then calculating its derivative with respect to X recovers the time-dependent variational principle as formulated in Ref. [12]. The tensor X is to be compared with that in Ref. [12] rescaled by the square root of the environment tensor. The quickest route to see this is to expand the circuit to quadratic order in the tensor X and bi-linear order in X and dt , before differentiating with respect to X .

3. Optimising Quantum Circuits

Our algorithms require the optimisation of expectations of observables — in Figs. 2b), and 3a) — and the solution of fixed point equations in Figs. 2b), and 3b) and c) to determine the environment and mixed environment. In all cases, optimisations are carried out stochastically.

We use the Rotosolve algorithm[37] to speed up our stochastic searches. This utilises the fact that the dependence of expectations

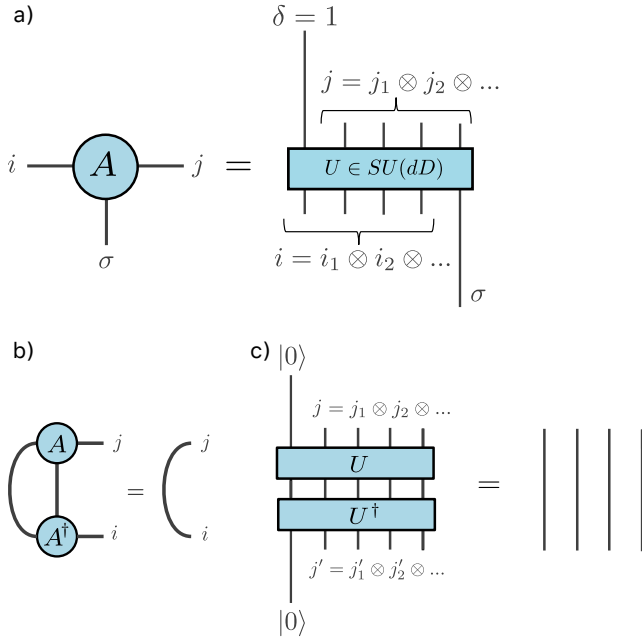


FIG. 6. **Translation between MPS quantum circuits:** a) The translation of an MPS tensor to a quantum circuit. The auxiliary index of bond order D is created from $N = \log_2 D$ qubits. b) The canonical form implies that the effect of contracting the MPS to the left is trivial. c) With our mapping of the MPS to a quantum circuit, the unitarity of U automatically puts the tensor in left canonical form.

of a parametrized quantum circuit on any particular parameter is sinusoidal. As a result, after just three measurements one can take this parameter to its local optimum value. Extensions of this allow the variation to be calculated when several elements of the circuit depend upon same parameter.

The equations illustrated in Figs. 2b), and 3b) and c) are implicitly identities between density matrices. We solve them using a version of the swap test that amounts to a stochastic optimisation of the objective function $\text{tr}[(\hat{r} - \hat{s})^\dagger(\hat{r} - \hat{s})]$. Details of how the swap test is implemented for the environment in Fig. 2b) and for the mixed environments in Figs. 3b) and c) are given in the supplementary materials.

Appendix B: Supplementary Materials

In this supplementary material we further explain the methods used in the quantum circuit implementation of iMPS algorithms, and the effects of imperfections in that realisation. We begin by giving details of the algorithms used to determine the unitaries required to represent and optimize quantum matrix product states. We then present some optimizations that can be used to attain significant reductions in numbers of parameters and optimization time - first we detail appropriate ansätze, then we give the details of an optimization method we have found effective. Next we detail the natural generalisation to higher bond order matrix product states, before giving additional data on the effects of shallow circuit realisations and finite gate fidelity. Finally, we explain the simulation and error mitigation methods we have used to simulate systems exhibiting many-body scars.

1. Finding the Environment

In order to determine the environment on the quantum chip we need to implement the equality of Fig. 2 from the main paper. Fig. 7 details the quantum circuits required to do so. We use the SWAP test [38] to compare both sides of the equation. The minimal application of this is illustrated by the circuit shown in Fig. 7b. However, the overlap $F(\rho, \sigma) = \text{tr}(\rho\sigma)$ is not necessarily maximised by $\rho = \sigma$. In fact, $F(\rho, \rho) = \text{tr}(\rho^2)$ is the purity, so that if the reduced density matrices of Fig. 7b are mixed. The optimizer will incorrectly try to increase the purity. We circumvent this by using a quantity related to the trace distance $\text{tr}((\rho - \sigma)^\dagger(\rho - \sigma))$, which is minimized at $\rho = \sigma$. The circuits required to determine the trace distance are shown in Figs. 7a and c.

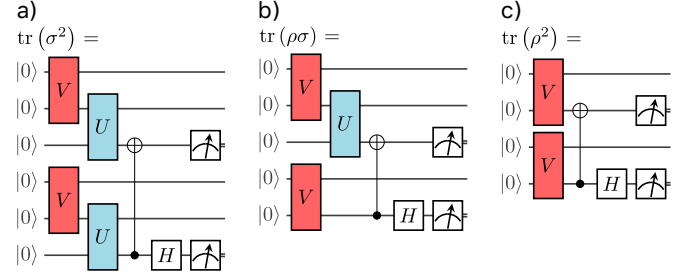


FIG. 7. **Quantum circuits to find the environment:** In order to determine an approximation to the overlap, the fraction of 00 outputs is measured on the measurement symbols.

2. Finding the Overlap

In order to time evolve a matrix product state on a quantum computer, we minimize the overlap between the perfect evolution of the state from time t to $t + \delta t$ and the manifold of matrix product states of the available bond dimension. In the infinite translationally invariant case, the definition of the overlap requires care. It can be given as the largest eigenvalue of the *mixed transfer matrix*.

a. The overlap as largest eigenvalue

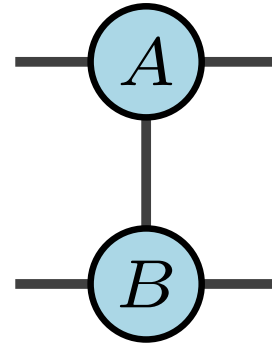


FIG. 8. **The mixed transfer matrix**

The overlap is the result of applying the matrix of Fig. 8 an infinite number of times to boundary vectors. The result (with appropriate normalisation) is equal to the largest eigenvalue. In order to find the largest eigenvalue, we use a variational method

to find the largest eigenvalue-eigenvector pair. Since the matrix in Fig. 8 is not Hermitian, we cannot use the Rayleigh-Ritz variational principle. Instead, we minimize the distance between the result of applying the transfer matrix to a vector, and the product of that vector with a candidate eigenvalue. Denoting the matrix of Fig. 8 as E_B^A , we seek to solve:

$$\max_{\eta} \min_r \left\| E_B^A r - \eta r \right\|^2. \quad (\text{B1})$$

In the applications considered in this work, we need only the overlap between very similar states, and can take advantage of the fact that we know that η can deviate from 1 only by a correction of order δt . As a result, we have found it effective to apply a heuristic, wherein we minimise over both η and r , using an appropriate initial condition for $\eta \sim 1$, and restart the optimization if it fails to attain $\eta \sim 1$ at its conclusion:

$$\min_{\eta, r} \left\| E_B^A r - \eta r \right\|^2 = \min_{\eta, r} v(\eta, r), \quad (\text{B2})$$

where we have defined our objective function $v(\eta, r)$. In practice, only rarely are repetitions required to find the largest eigenvalue and even then a small number of repetitions suffices (See Fig. 9).

b. Solving Eq. (B2) on a quantum circuit

Expanding Eq. (B2) allows us to put it in a form that can be implemented as quantum circuits:

$$v(\eta, r) = r^\dagger E_B^{A\dagger} E_B^A r + |\eta|^2 r^\dagger r - r^\dagger E_B^A r - r^\dagger E_B^{A\dagger} r. \quad (\text{B3})$$

The first two terms can be implemented on quantum circuits as shown in Figs. 10d and 10f (a and b for the corresponding left eigenvectors). The objective function is found by measuring in the computational basis, determining the probability of the bit string of all 0s, and taking the square root of the corresponding probability (since we know the result should be real, there is no problem determining the phase). The same is not true of the third and fourth terms of Eq. (B3), for which there is an undetermined phase. At the minimum, the sum of the last two terms will be equal to the largest eigenvalue, which is real to $O(dt^2)$, since the largest eigenvalue of E_A^A is 1. Therefore, if we minimize the associated objective function:

$$v'(\eta, r) = r^\dagger E_B^{A\dagger} E_B^A r + |\eta|^2 r^\dagger r - 2 \left| r^\dagger E_B^A r \right|, \quad (\text{B4})$$

by taking the square root of the corresponding probabilities (Fig. 10 b and e), the argmin will coincide with that of Eq. (B2) (to $O(dt^2)$), and we can determine the eigenvalue and eigenvector. In practise, we often achieve an accuracy much greater than $O(dt^2)$. Fig. (9) gives data demonstrating the accuracy and reliability of this method of determining the overlap.

3. Ansätze

Implementation of iMPS algorithms on quantum computers require factorisations of the large unitaries in which the tensors are embedded. Different ansätze make different tradeoffs between gate depth, gate availability on typical QC implementations, and expressibility. The different unitaries (U and V , containing the state tensor and the environment tensor respectively), can be factorised in different ways, to take into account their different structures. At low bond dimension, full parametrisations of the important matrix spaces are possible.

a. The state unitary U

For this work, we used the generic ansatz for U reported in Fig. 4a in the main body of the paper. We found it to be a workable tradeoff between expressibility and depth in the generic case. However, ground state problems like this often have some deeper structure, and that structure can be exploited for more efficient circuit ansätze, and more effective optimization.

As an example, the transverse field Ising model used as an example in the main text exhibits time reversal invariance, parity symmetry, and has a conserved quantity (the total magnetization). While in Fig. 4b in the main text we use the general ansatz of Fig. 4a,

These properties constrain the form of the true ground state of the system, and its MPS approximation. The transverse field Ising model Hamiltonian is real, and thus the model exhibits time reversal invariance. The MPS form of the ground state should be made up of real tensors [39]. In Fig. 11, we demonstrate the

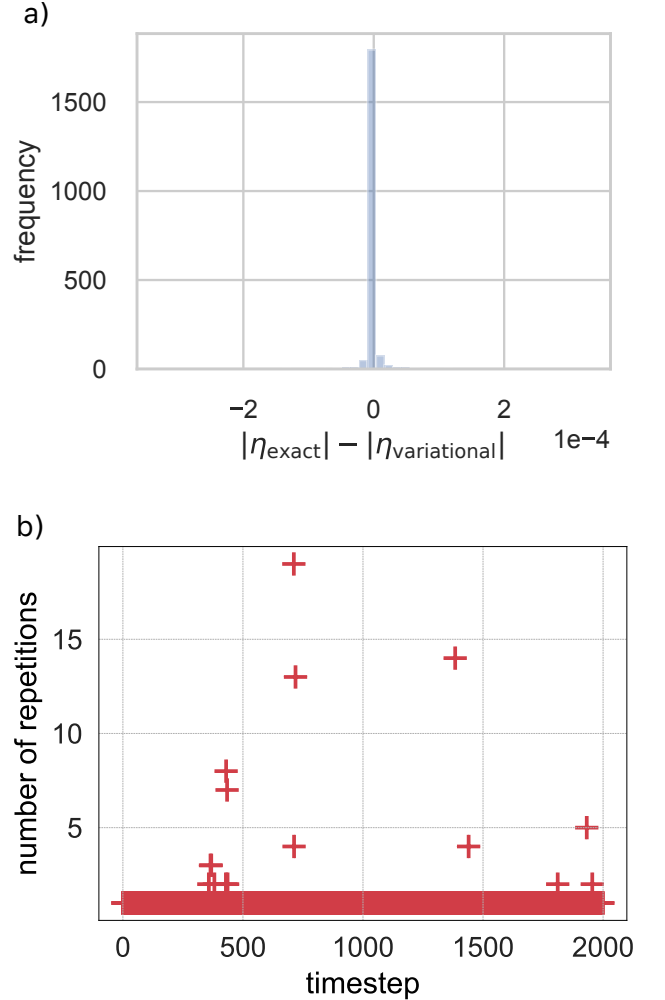


FIG. 9. **Performance of finding the right environment with Eq. (B4)** a) Distribution of results of minimizing Eq. (B4): a comparison of the exact and variational largest eigenvalue of the mixed transfer matrices for 2000 steps along a TDVP trajectory, with $\delta t = 0.01$, using the BFGS optimizer provided in scipy. b) Number of repetitions vs. time: Number of repetitions required at each timestep in (a).

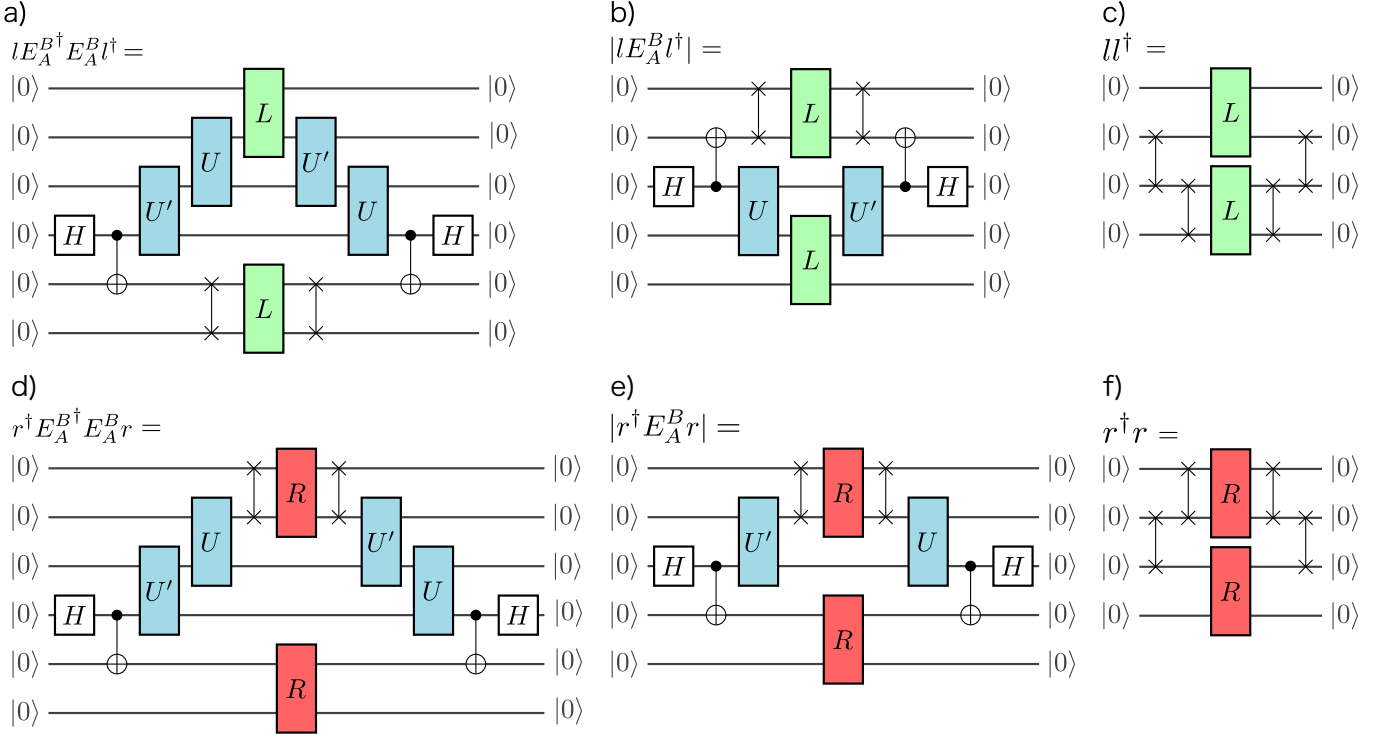


FIG. 10. **Diagrams required for the mixed environment.** The probability of measuring the all 0s bit string is measured on all the above circuits, then the real square root is taken to calculate the labelled expression.

resulting speedups for two different real ansätze. Note in particular that for the ansatz of Fig. 11, the optimization produces optimal results (i.e. equivalent to D=2 classical), for a state tensor of only depth 4.

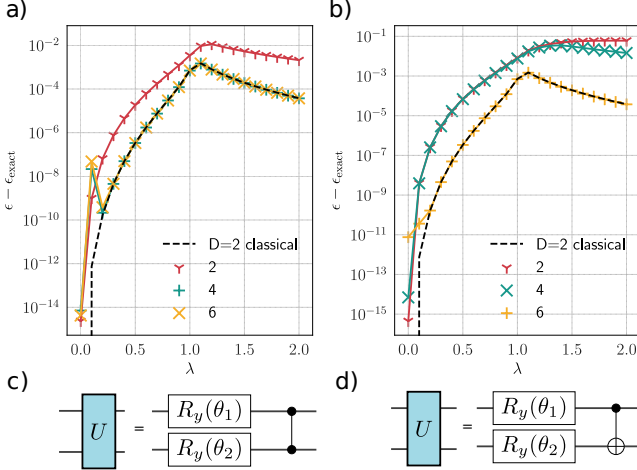


FIG. 11. **Time Reversal Symmetry in optimization of the transverse-field Ising model:** a) and b) Deviation from analytical ground state energy density of the transverse-field Ising model as a function of λ . Dashed line is the result of classical iDMRG at D=2, other lines/markers are the result of quantum variational optimization at different ansatz depths, given in the legend. c) and d) Ansatzes used to produce figures a) and b), respectively.

b. Representing the environment

The simulations presented in the main paper were performed at $D = 2$. At $D = 2$, the depth required for a full parametrisation of the environment is easily accessible, and a minimal parametrisation is available. The resulting circuits allow us to calculate important quantities (the Schmidt coefficients, for example) classically, and point the way to natural generalisations for $D > 2$.

A full parametrisation of the right environment at $D = 2$

The environment - the right fixed point, r , of the MPS transfer matrix [16] - is an Hermitian, positive definite matrix, with trace 1. V embeds the Cholesky decomposition of the right environment in a unitary. To obtain the right environment, we parametrise V as shown in Fig. 12.

Since the environment r has trace 1, the Cholesky factor $r^{\frac{1}{2}}$ has Frobenius norm 1. First consider the matrix in Fig. 12a. This spans all possible diagonal environment square roots, since $\text{tr}(D^\dagger D) = 1$, $D^\dagger D \geq 0$, and $\cos(\gamma)$ is surjective onto $[-1, 1]$, where $D(\gamma)$ is defined in Fig. 12. Any 2×2 Hermitian, unit trace matrix can be written as $U D(\gamma)^\dagger D(\gamma) U^\dagger$ for some U and γ . An arbitrary unitary on 1 qubit is shown in Fig. 12b. Since diagonal matrices commute, the unitary of Fig. 12c suffices for V .

This parametrisation has some advantages:

- It is minimal, depending upon only 3 real parameters;
- The eigenvalues of the environment are classically accessible. The purity, Von Neumann entanglement entropy *etc.* are all accessible with simple calculations if we know the parameters of the ansatz.

Alternative representations of the environment When considering the quantum circuits used to implement the time-dependent variational principle, it is convenient to use a different representation of the environment as indicated in Fig. 13a. This restructuring allows us to trade depth for qubits, and makes manifest the time reversal symmetry of the TDVP circuits. It also allows us to explore non

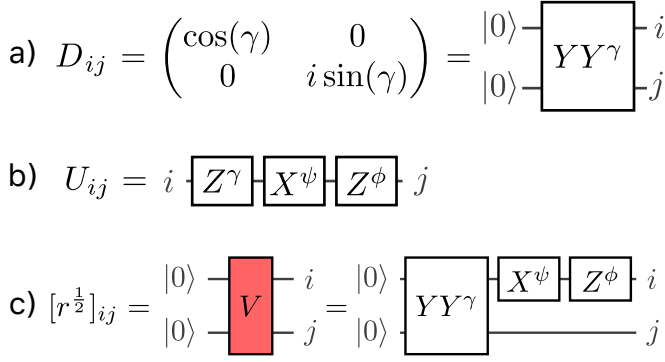


FIG. 12. Parametrisation of the environment V , used throughout

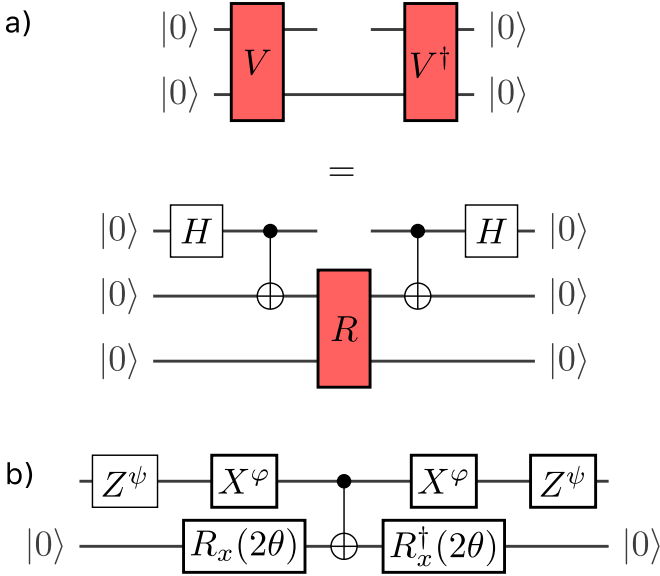


FIG. 13. a) The alternative representation of the environment, used in the TDVP circuits and b) the corresponding full parametrisation of the unitary R .

Hermitian tensors variationally. This is crucial in the calculation of the overlap. The parametrisation of the tensor R (Fig. 13b) retains the benefits of the parametrisation of Fig. 12c, in particular, the eigenvalues of the environment (the square of the Schmidt coefficients across each bond) are: $\lambda_1 = \cos^2(\theta)$, $\lambda_2 = \sin^2(\theta)$.

4. Optimization Methods

Variational algorithms require the use of effective optimization algorithms. In the main text, we have made use of several - the standard algorithms provided in `scipy`, and a coordinate optimization method named Rotosolve. In this section we detail a necessary modification to the Rotosolve algorithm, and compare the performance of each on our setup.

Doubled Rotosolve: Rotosolve is an optimization method for quantum circuits. As detailed in Ref. [37], it takes advantage of the fact

that for quantum circuits $U(\vec{\theta})|0\rangle$, in which each θ_k parametrises a single exponential of a Pauli string ($e^{-i\theta_k S}$, $S^2 = I$), the expectation values of local observables must vary sinusoidally as a function of θ_k . The details of the resulting sinusoid can be determined by three measurements at different values of θ_k , and once determined, the minimum for that parameter (for the current values of the rest of $\vec{\theta}$) can be attained immediately. Analytic gradient methods like Rotosolve can lead to dramatic ($\sim 100\times$) reduction in the number of measurements required to optimize a circuit.

Rotosolve as introduced in Ref. [37] requires that each parameter control at most one gate. For circuits such as those shown in Figs. 7a-c), where each parameter controls more than one gate, a small modification to the Rotosolve algorithm is necessary.

Doubly Sinusoidal Expectation Values: A derivation of the original Rotosolve algorithm is given in the appendix of Ref. [37]. Here we present a brief extension of this derivation to the situation where a given parameter controls two gates. Consider a generic quantum circuit, in which each element is the parametrised exponential $U_i = e^{-i\theta_i S_i}$ of some Pauli string S_i , $i \in [1 \dots N]$, $S_i^2 = I$. Consider the expectation value of an operator \hat{O} in the output of this circuit, as a function of one of the θ_i , in a circuit consisting of N gates depending on $M < N$ parameters, where at most two identical gates U_k depend upon the same parameter θ_k . Using the expansion $U_k(\theta_k) = e^{-i\theta_k S_k} = \cos(\theta_k/2)\mathbb{I} + \sin(\theta_k/2)S_k$, and defining the quantities:

$$A = \langle \hat{O} \rangle_{\theta_k=0} + \langle \hat{O} \rangle_{\theta_k=\pi}, \quad (\text{B5})$$

$$B = \langle \hat{O} \rangle_{\theta_k=0} - \langle \hat{O} \rangle_{\theta_k=\pi}, \quad (\text{B6})$$

$$C = \langle \hat{O} \rangle_{\theta_k=\pi/2} + \langle \hat{O} \rangle_{\theta_k=-\pi/2}, \quad (\text{B7})$$

$$D = \langle \hat{O} \rangle_{\theta_k=\pi/2} - \langle \hat{O} \rangle_{\theta_k=-\pi/2}, \quad (\text{B8})$$

$$E = \langle \hat{O} \rangle_{\theta_k=\pi/4} - \langle \hat{O} \rangle_{\theta_k=-\pi/4}, \quad (\text{B9})$$

and the combinations:

$$a = \frac{1}{4}(2E - \sqrt{2}D), b = \frac{1}{4}(A - C), c = \frac{1}{2}D, d = \frac{1}{2}B,$$

one can show that:

$$\begin{aligned} \langle \hat{O} \rangle_{\theta_k} &= a \sin(2\theta_k) + b \cos(2\theta_k) + c \sin(\theta_k) + d \cos(\theta_k) \\ &= P \sin(2\theta_k + \phi) + Q \sin(\theta_k + \psi) \end{aligned} \quad (\text{B10})$$

where $P = \sqrt{a^2 + b^2}$, $\phi = \arctan_2(a, b)$, $Q = \sqrt{c^2 + d^2}$, $\psi = \arctan_2(c, d)$. Unlike the original Rotosolve algorithm, Eq. (B10) is not a single sinusoid but a sum of sinusoids with doubled frequencies and different amplitudes and phases. It can no longer be minimized analytically. However, the spirit of the Rotosolve algorithm remains, and one proceeds as follows:

1. Perform the 6 measurements required to determine A, B, C, D, E .
2. Perform a classical scalar minimization on the function $\langle \hat{O} \rangle_{\theta_k}$ (whose coefficients have now been determined). This can be done very quickly on the fly, or precomputed and interpolated for arbitrary P, Q, ϕ, ψ .
3. Set the variable θ_k to its corresponding minimum.

The resulting algorithm suffers no significant loss of performance over Rotosolve, and only requires 3 more measurements per iteration.

5. Higher Bond Order Circuits

The simulations presented in the main body of the paper are carried out for $D = 2$. This is mainly to obtain compact circuits

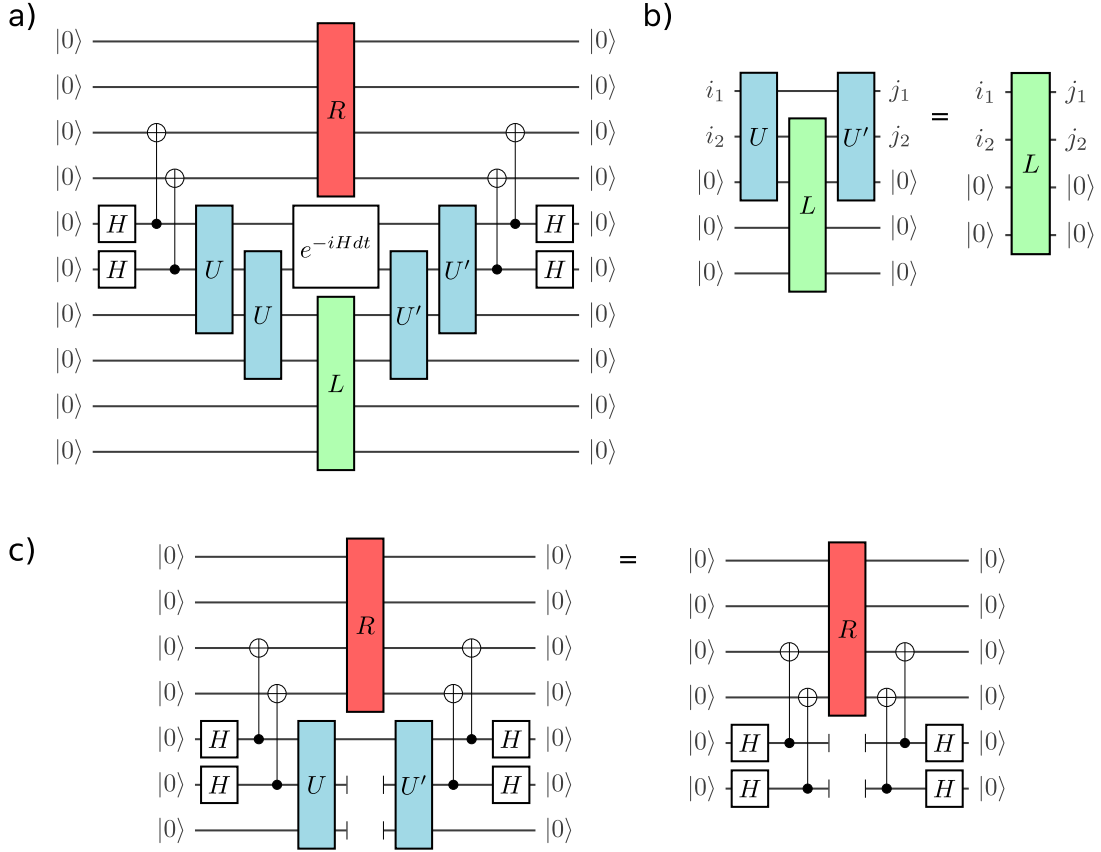


FIG. 14. **Quantum Implementation of the Time-dependent variational principle at $D=4$:** The equivalent circuits to those shown in Fig. 3 of the main text at $D = 2$ are shown here at $D = 4$. a) The time-dependent variational principle is implemented by optimising the overlap of the output of this circuit with $|000\dots\rangle$. b) and c) give the fixed point equations for the mixed left and right environments (Fig. 3 in the main text) are shown in Fig. 14.

that are feasible to implement on available (or imminently available) NISQ machines. Our code (in both Cirq and Qiskit) can run with arbitrary bond order. By way of illustration, the circuits implementing the time-dependent variational principle and fixed point equations for the mixed left and right environments (Fig. 3 in the main text) are shown in Fig. 14.

6. Finite Gate Fidelity and Restricting Circuit Depth

Finite gate-fidelity implies a maximum reliable depth of quantum circuit. As evident from Figs. 2 and 3, passing from the simplest task of representing a quantum state through the more complicated tasks of optimising and time-evolving states, the required circuits are broader and of greater depth. Time-evolution is therefore much more susceptible to gate errors than simply representing a state. Whilst it might be possible to represent and measure properties of a rather high bond-order state, time-evolution is inevitably restricted to lower bond order.

Fig. 15a shows how the attainable groundstate fidelity of the transverse-field Ising model $\mathcal{H} = \sum_i \sigma_i^z \sigma_{i+1}^z + \lambda \sigma_i^x$ changes with λ for fixed noise strength $\eta = 1 \times 10^{-3}$. The same gate fidelity has a much more severe effect upon simulations of dynamics. Fig. 15b shows how a simulation at $D = 2$ is degraded by this error rate.

This formalism allows us to make a variety of tradeoffs between noise and performance, depending upon the resources available on

the quantum computer. One can increase the expressibility of the circuit by increasing the depth of the ansatz. It is also possible to modify the variational space by using a shallow ansatz at a larger bond order, which requires a greater qubit count. It remains to be seen how each of these options will perform on a near term chip.

7. Many Body Scars

In the main text, we have proposed the study of many-body quantum scars as a potentially challenging use of NISQ machines. The representation of this physics by a Poincaré map, requires accurate simulation of time evolution over long times. The finite time-step in such a simulated evolution and finite gate errors can lead to two types of error in the construction of the map.

a. Poincaré Maps from Discrete Timeseries

To produce a Poincaré map, the parameters that define the quantum state are recorded as they evolve over time. When a chosen parameter crosses a particular value in the positive direction the values of the other parameters are plotted. The values of these crossings indicated in Fig. 5c of the main text are obtained by polynomial interpolation of the values at discretised time intervals obtained from the quantum circuit. This proceeds as follows: Around the approximate crossing time, polynomial function inter-

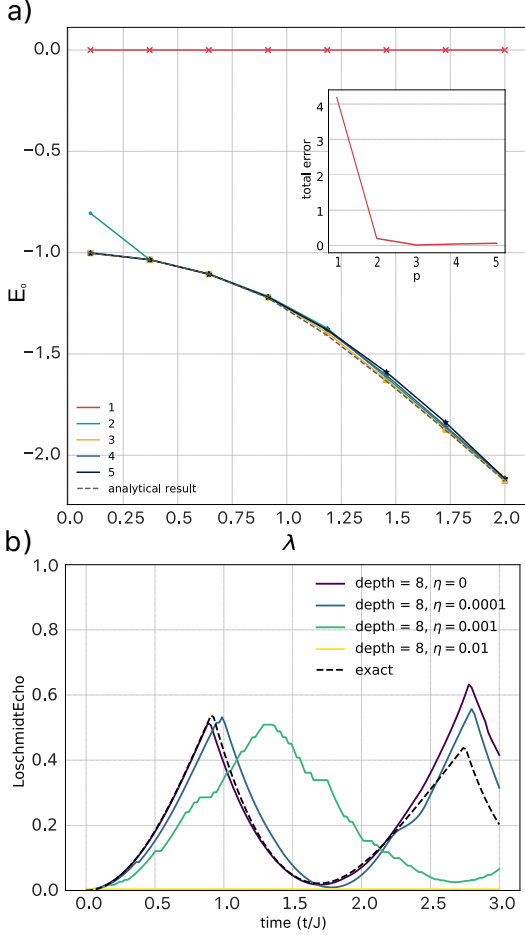


FIG. 15. **Effect of finite gate fidelity upon optimisation and evolution:** a) Effect of noise upon time evolution, η is depolarising probability. Increasing noise deteriorates but does not destroy the appearance of the dynamical phase transition peaks. b) Optimization, for depolarising probability $\eta = 1 \times 10^{-3}$, and varying circuit depth (legend). Inset shows total deviation from exact curve as a function of depth (p). Note the tradeoff between circuit depth and sensitivity to noise. For computational expediency, expectation values are calculated exactly from noisy circuits.

polution is used to estimate the evolution of all parameters. A root finding algorithm is used on the interpolated polynomial function of the chosen parameter to get an estimated time of crossing. Finally this time is input into the other interpolated functions to get estimates of all the parameters at the crossing time.

b. Error Mitigation

The finite time-step and finite gate fidelity also lead to errors in the integration of the implied equations of motion[40]. A simple method to reduce these errors is to post select on a quantity that should be conserved along correct trajectories. Evolution under the time-dependent variational principle conserves energy. As errors accumulates the energy drifts from this original fixed value. Using post-selection to retain trajectories that preserve the energy

to some accuracy provides a simple way to mitigate these errors. This post-selection doesn't correct the errors entirely but the important structures in the maps might be better preserved.

However, the dynamics at certain values of the variational parameters may be trickier to simulate with errors occurring at a faster rate. if this is not accounted for, post-selection will remove these regions from the Poincaré map. To address this a flexible energy window can be used where a different accuracy is demanded in different regions of the map in order to keep the same fraction of points in each section. In this work we have simply divided the phase space of the Poincaré map into the quadrants illustrated in Fig. 16. To produce Fig. 5c in the main text, we divided the time evolution into four stages. In each stage we time-evolved for $t = 10$ (in units of the Hamiltonian given in Fig. 5 in the main text) post-selecting after each as described in Fig. 16.

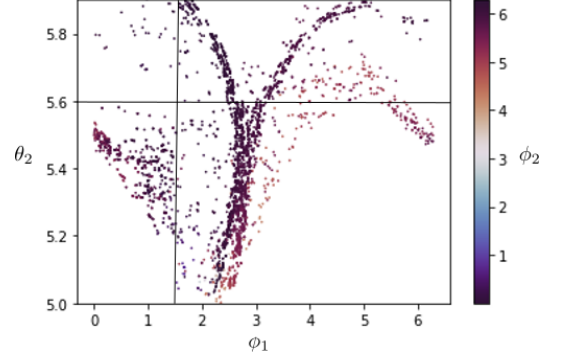


FIG. 16. **Quadrants imposing different accuracy of energy conservation for post-selection.** In each quadrant, the 10% of points that best conserve energy are retained and are used to seed further trajectories. This post-selection is carried out over 3 stages of time evolution. At the final stage, the best $\frac{2}{3}$ of points are retained to produce the figure.

8. Code Availability

All code used to generate the results presented is available to download at <https://github.com/fergusbarratt/qmps>. We provide both Cirq code — which we have used in our simulations — and Qiskit code with the same functionality.